LETTERS
PUBLISHED ONLINE: 16 DECEMBER 2012 | DOI: 10.1038/NNANO.2012.220
nature nanotechnology

Electrostatic assembly of binary nanoparticle superlattices using protein cages

Mauri A. Kostiainen[1]*, Panu Hiekkataipale[1], Ari Laiho[2], Vincent Lemieux[3], Jani Seitsonen[1], Janne Ruokolainen[1] and Pierpaolo Ceci[4]

Binary nanoparticle superlattices are periodic nanostructures with lattice constants much shorter than the wavelength of light[1,2] and could be used to prepare multifunctional metamaterials[3,4]. Such superlattices are typically made from synthetic nanoparticles[5–8], and although biohybrid structures have been developed[9–15], incorporating biological building blocks into binary nanoparticle superlattices remains challenging[16–18]. Protein-based nanocages provide a complex yet monodisperse and geometrically well-defined hollow cage that can be used to encapsulate different materials[19,20]. Such protein cages have been used to program the self-assembly of encapsulated materials to form free-standing crystals[21,22] and superlattices at interfaces[21,23] or in solution[24,25]. Here, we show that electrostatically patchy protein cages—cowpea chlorotic mottle virus and ferritin cages—can be used to direct the self-assembly of three-dimensional binary superlattices. The negatively charged cages can encapsulate RNA or superparamagnetic iron oxide nanoparticles, and the superlattices are formed through tunable electrostatic interactions with positively charged gold nanoparticles. Gold nanoparticles and viruses form an AB_8^{fcc} crystal structure that is not isostructural with any known atomic or molecular crystal structure and has previously been observed only with large colloidal polymer particles[26]. Gold nanoparticles and empty or nanoparticle-loaded ferritin cages form an interpenetrating simple cubic AB structure (isostructural with CsCl). We also show that these magnetic assemblies provide contrast enhancement in magnetic resonance imaging.

Native cowpea chlorotic mottle virus (CCMV) is a small icosahedral virus (diameter $D \approx 28$ nm) consisting of 180 identical coat protein subunits that form a Caspar–Klug triangulation number $T = 3$ capsid around three (+)ssRNA strands (Fig. 1a,d). The ferritin (FT) used in this work is a recombinant protein cage from hyperthermophile *Pyrococcus furiosus* and has a hollow cavity (apoFT) for hosting superparamagnetic Fe_3O_4–γ-Fe_2O_3 iron oxide (MF)[27]. The FT cage comprises an assembly of 24 protein subunits that form a hollow globular shell ($D_{FT} \approx 12$ nm) with 432-pointgroup symmetry (Fig. 1b,d). Both CCMV and FT cages carry a negative net charge on their outer surfaces at neutral pH (isoelectric point, pI ≈ 3.8 and 4.5, respectively). The negative charge density on CCMV and FT is not homogeneously distributed, but is located in patches on the cage surface. The presence of directional 'sticky patches' can direct nanostructure formation, which is controlled by interactions between the patches[28–31]. 1-Pentanethiol-stabilized gold nanoparticles (AuNPs) were prepared according to the biphasic Brust method (Supplementary Section S1). Subsequent ligand exchange yielded final AuNPs carrying multiple quaternary amine groups, which remain cationic over a wide pH range (Fig. 1c,d). Based on transmission electron microscopy (TEM) and dynamic light scattering (DLS) experiments, the metallic cores of the AuNPs were found to have an average diameter of 2.6 nm, whereas the average diameter of the ligand-stabilized AuNPs was ~8.5 nm. All the building blocks were radially symmetric and the size ratios of the AuNPs and protein cages ($\gamma = D_{AuNP}/D_{pc}$) were ~0.30 and ~0.71 for CCMV and FT, respectively.

The self-assembly of three-dimensional binary nanoparticle superlattices requires careful tailoring of the particle–particle interactions to a regime that is on the order of k_BT (k_B = Boltzmann constant, T = absolute temperature). Strong attraction between the particles leads to gel-like aggregates without periodic order. On the other hand, weak interparticle interactions fail to produce any assemblies[5,32]. The length over which the electrostatic interactions between the particles are effective in solution is given by the Debye screening length

$$\kappa^{-1} = \sqrt{\frac{\varepsilon_0 \varepsilon_r k_B T}{e^2 \sum_i c_i z_i^2}}$$

where ε_0 is vacuum permittivity, ε_r is the dielectric constant of the solvent (here H_2O), e is the elementary charge, and c_i and z_i are the number densities and valencies of the electrolyte ions (here NaCl, KCl or $MgCl_2$). Because the ionic strength of the solvent media strongly affects the extent of Coulombic interactions, κ^{-1} was tuned by controlling the concentration of the electrolyte. On the other hand, the magnitude and sign of the charge of the protein cage could be controlled by adjusting the pH. By controlling the electrolyte concentration and pH we were therefore able to adjust the attraction between CCMV and AuNPs to a regime where superlattice formation was possible.

Small angle X-ray scattering (SAXS) measurements were carried out on aqueous samples containing different AuNP/CCMV ratios, NaCl concentrations and pH values. Figure 2a shows how the sample crystallinity depends on κ^{-1} and pH, as measured by SAXS. Three distinct regions can be defined: amorphous gel-like (region 1), crystalline (region 2) and free particles (region 3). At constant pH 5 (Fig. 2a, top), superlattices are obtained with various AuNP/CCMV ratios, but only when $\kappa^{-1} \approx 1.2$–0.8 nm (region 2). When pH < pI, CCMV gains a positive net surface charge, and electrostatic superlattice formation with cationic AuNPs at a mass ratio of 0.75 is not possible (Fig. 2a, bottom). For pH > pI, CCMV particles are negatively charged and superlattices can be observed. The

[1]Molecular Materials, Department of Applied Physics, Aalto University, 00076 Espoo, Finland, [2]Advanced Magnetic Imaging Centre, O.V. Lounasmaa Laboratory, School of Science, Aalto University, 00076 Espoo, Finland, [3]St-Jean-Photochimie (SJPC), 725 Trotter Street, Saint-Jean-sur-Richelieu, Quebec J3B 8J8, Canada, [4]National Research Council of Italy (CNR), Institute of Molecular Biology and Pathology, 00185 Rome, Italy.
*e-mail: mauri.kostiainen@aalto.fi

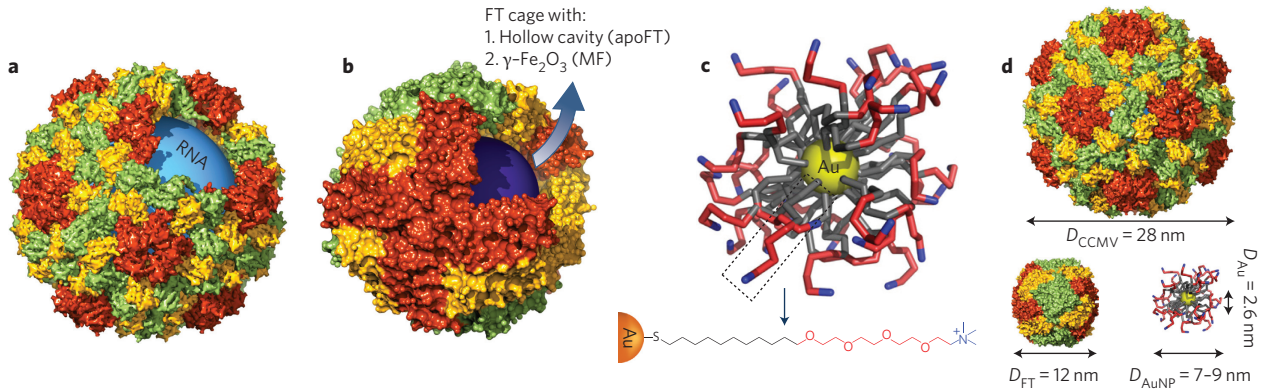

Figure 1 | Materials used for the assembly of binary protein cage–nanoparticle superlattices. a, Native CCMV with RNA genome inside. **b**, Apoferritin and magnetoferritin (recombinant ferritin cage from *Pyrococcus furiosus* encapsulating Fe_3O_4–γ-Fe_2O_3). **c**, Gold nanoparticle stabilized with an amphiphilic ligand featuring a cationic quaternary amine end-group. **d**, Size of the building blocks drawn to scale.

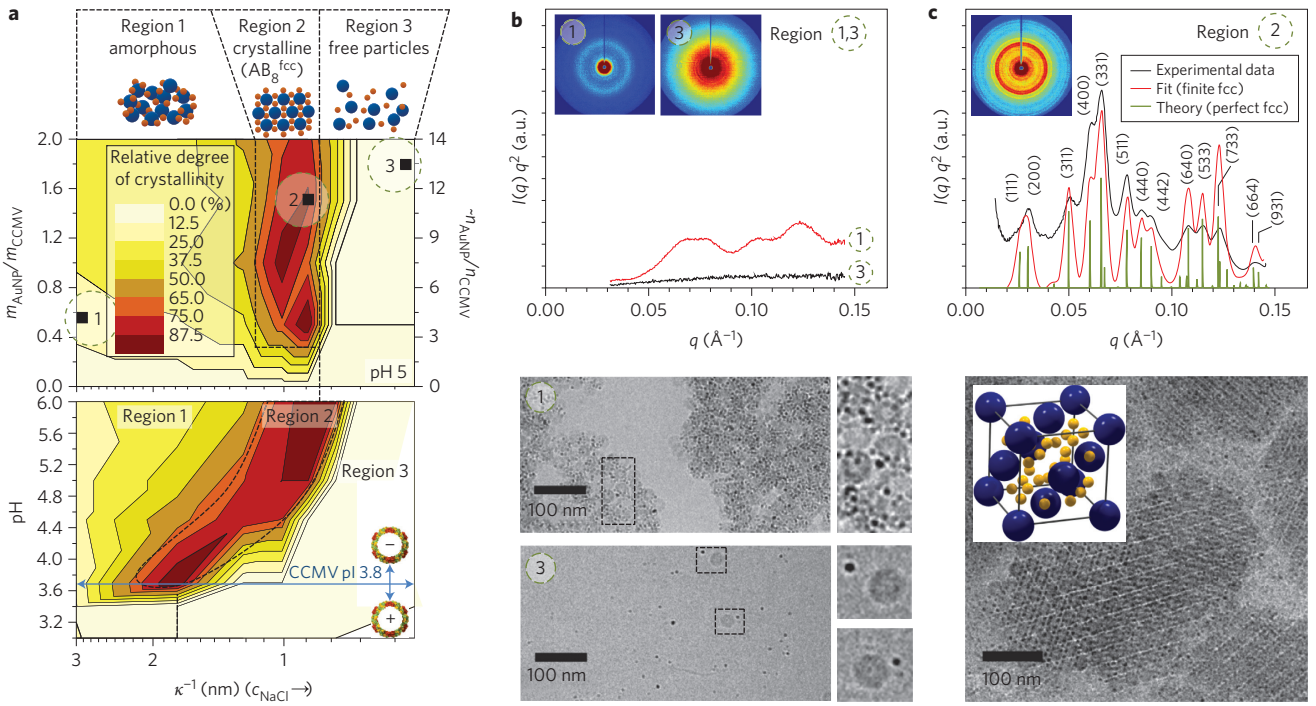

Figure 2 | Self-assembly of three-dimensional binary CCMV–AuNP superlattices. a, Superlattice formation at different Debye screening lengths κ^{-1} (adjusted by NaCl concentration), AuNP/CCMV mass ratios (top) and pH values (bottom) studied by SAXS. At low NaCl concentration only amorphous gel-like aggregates are observed (region 1). At a given pH the superlattice formation is efficient only in a narrow NaCl concentration window (region 2), which is shifted to smaller κ^{-1} when pH is increased. Superlattice formation is possible only when pH > pI of CCMV. High NaCl concentration screens the electrostatic interaction, yielding only individual free particles (region 3). **b**, Two- (insets) and one-dimensional SAXS patterns for samples (1) and (3) show scattering from amorphous aggregates and free particles, respectively. Cryo-TEM images of the respective samples are shown below. **c**, Two-dimensional (inset) and integrated one-dimensional SAXS data for crystalline protein cage–nanoparticle superlattices (sample 2) indexed with AB_8^{fcc}-type lattice (top). The experimental scattering pattern (black trace) matches well with the respective theoretical scattering pattern (red and green traces). Crystalline superlattices are also observed with cryo-TEM. The particles arrange into an AB_8^{fcc}-type lattice (bottom), where CCMV adopts an fcc structure and the voids between the CCMVs are filled with eight AuNPs. A model unit cell is shown in the inset (CCMV, blue spheres; AuNP, yellow spheres; the radii of the particles have been reduced by 50% for clarity).

magnitude of the negative charge on the CCMV and the electrostatic interaction with the AuNPs increases with increasing pH, so shorter screening lengths are needed to suppress the aggregation and bring the system to a weakly attracting regime. This is observed as a shift in the κ^{-1} window for superlattice region 2 to shorter screening lengths (Fig. 2a, bottom).

Two-dimensional SAXS data and integrated one-dimensional curves selected from regions 1 and 3 do not show distinct scattering patterns (Fig. 2b, top). Cryogenic transmission electron microscopy (cryo-TEM) images of these samples also show amorphous gel-like and free particles respectively, both in good agreement with the SAXS data (Fig. 2b, bottom). The fact that the particles can be fully dissolved at high salt concentrations indicates that the van der Waals interactions between the particles are weak.

In the samples containing crystalline assemblies (region 2), the two-dimensional scattering pattern shows the most prominent

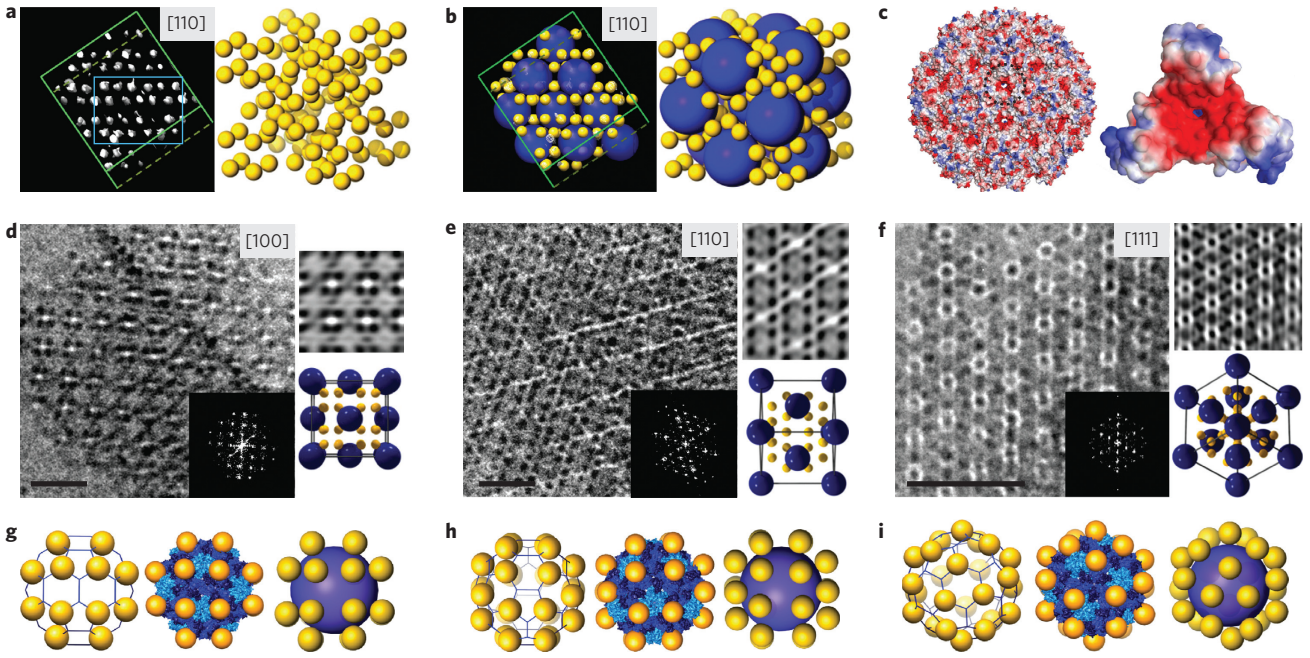

Figure 3 | TEM characterization of the AB_8^{fcc}-type $(CCMV–AuNP_8)^{fcc}$ superlattice. a, Three-dimensional electron density maps obtained by cryo-ET. Left: $(CCMV–AuNP_8)^{fcc}$ superlattice viewed along the [110] zone axis. Unit cell is outlined in cyan. Right: position of the AuNPs mapped with the help of the electron density map. **b**, The respective electron density maps as shown in **a** mapped with the CCMV (blue) and gold (yellow) nanoparticles. **c**, Left: crude electrostatic potential of the CCMV capsid viewed along the two-fold symmetry axis shows 60 negative patches located around the pore at the quasi-three-fold axis. Right: magnified view of one of the negative patches. Values range from 0 (blue) to $-9k_BT/e$ (red). **d–f**, Cryo-TEM images of vitrified aqueous solution containing superlattices viewed along [100] (**d**), [110] (**e**) and [111] (**f**) projection axes show a high degree of ordering. Each panel contains a cryo-TEM image (scale bar, 50 nm), image Fourier transform (inset), inverse Fourier transform calculated with selected Fourier components (top right) and a unit cell viewed along the given projection axes (bottom right). The size of the particles has been reduced for clarity. **g–i**, Binding of 24 AuNPs on the negative patches viewed from the same directions as the TEM images above. Schematic frame (left) and surface presentation (middle) correspond to the experimental particle positions obtained by cryo-TEM tomography (right).

SAXS reflection from the $(hkl) = (331)$ plane at a magnitude of the scattering vector $q^{(331)} = 0.6777\ nm^{-1}$, giving $q^* = 0.1555\ nm^{-1}$. Multiple less intense reflections, for example at 0.3073, 0.5148, 0.6278 and 0.8011 nm^{-1} are also observed, which correspond to Bragg reflections from the (111) + (200), (311), (400) and (511) planes, respectively (Fig. 2c, top). The peak position ratios are $q^n/q^* \approx \sqrt{3}:\sqrt{4}:\sqrt{11}:4:\sqrt{19}:\sqrt{27}$, corresponding to a face-centred cubic (fcc) structure with $Fm\bar{3}m$ space group and a lattice parameter $a = 2\pi/q^*$ of 40.4 nm. The calculated $(a/\sqrt{2})$ centre-to-centre distance between the (111) plane CCMVs is 28.6 nm, which corresponds closely to the diameter of the virus particle. The relative heights and peak positions of the calculated theoretical SAXS curves are consistent with the experimental data. The superlattices are also clearly visible by cryo-TEM (Fig. 2c, bottom).

To confirm the SAXS measurements, cryogenic electron tomography (cryo-ET) was used to create electron density maps of the binary superlattices, and cryo-TEM was used to visualize the superlattices from different directions. The electron density map in Fig. 3a shows the position of electron-dense AuNPs along the [110] zone axis, indicating ordering in three dimensions. By mapping the voids between AuNPs with CCMV particles we obtained the same structure as observed by SAXS (Fig. 3b). The cryo-TEM images presented in Fig. 3d–f show the expected superlattice projections viewed along the [100], [110] and [111] zone axes, respectively. The lattice constant a determined from these images is 41.1 nm, in good agreement with the SAXS results.

Interestingly, in this assembly CCMV adopts an fcc structure where each octahedral void between the CCMVs is filled with a simple cubic (sc) arrangement of eight AuNPs (unit cell depicted in Fig. 2c inset). This superlattice is therefore comparable with a NaCl lattice, where the Na or Cl atoms are replaced by eight AuNPs in an sc arrangement. In total, the unit cell contains four CCMV particles and 32 AuNPs. We denote this structure as the $(CCMV–AuNP_8)^{fcc}$ superlattice, which is not isostructural with any known atomic or molecular crystal structure and has not previously been observed with nanosized particles. Such structures have been observed only in coexistence with the respective hexagonal close-packed (hcp) structure in organic solvents with much larger colloidal polymer particles ($D > 0.5\ \mu m$) and similar diameter ratios ($\gamma = 0.31$)[26,33]. Such observations were also supported by Monte Carlo simulations, suggesting that AB_8^{fcc}-type assemblies are indeed to be expected with high charge ratios[26]. The formation of $(CCMV–AuNP_8)^{fcc}$ superlattices is striking, because previous experimental and simulation works suggest that three-dimensional crystals are difficult to achieve from oppositely charged nanoparticles with different average sizes[34]. Here, the AuNPs and CCMV in particular have extremely low polydispersities, which helps to minimize entropic limitations related to the assembly process, and always results in the same $(CCMV–AuNP_8)^{fcc}$ superlattice with the studied AuNP/CCMV ratios, screening lengths and pH values.

The presence of negative surface patches can further guide superlattice formation. Large negatively charged patches, which can bind multivalent cations, are located around the 60 pores present in the centre of the three-fold quasi-icosahedral rotation axes (Fig. 3c). The distance between adjacent negative patches is ~6 nm, which indicates that two AuNPs with $D \approx 8$ nm are unable to bind to adjacent patches due to steric hindrance and electrostatic repulsion between the AuNPs. However, when AuNPs are mapped to the negative patches so that one empty patch is placed between the AuNPs, a total of 24 AuNPs can be placed in contact with one

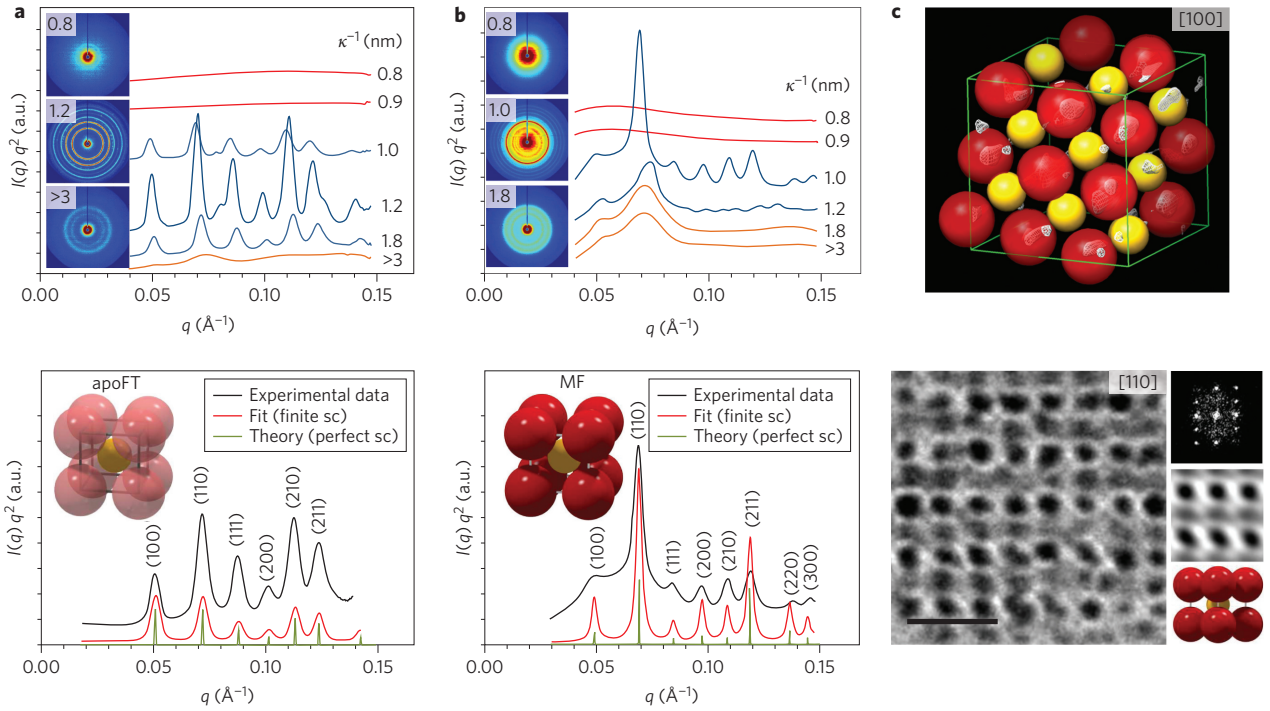

Figure 4 | Characterization of AB^{sc}-type (aFT–AuNP)^{sc} and (MF–AuNP)^{sc} superlattices. a,**b**, Top: one- and two-dimensional (insets) SAXS data for the formation of binary nanoparticle superlattices at different κ^{-1} (NaCl concentrations). Superlattice formation is efficient between 30 and 90 mM NaCl (**a**, corresponding to $\kappa^{-1} = 1.8-1$ nm) and at 90 mM NaCl (**b**, corresponding to $\kappa^{-1} = 1$ nm). Bottom: SAXS data for crystalline protein cage–nanoparticle superlattices indexed with AB^{sc}-type lattice. apoFT and gold nanoparticles (**a**) each form a separate simple cubic lattice that creates an interpenetrating structure with an apoFT particle at the centre of each AuNP cube ((aFT–AuNP)^{sc} superlattice). MF (**b**) creates a similar superlattice (MF–AuNP)^{sc} that is isostructural with CsCl. A model unit cell is shown in the inset (AuNP, yellow sphere; apoFT, transparent light red spheres; MF, solid red spheres). **c**, Top: three-dimensional electron density map obtained by cryo-ET of the (MF–AuNP)^{sc} superlattice mapped with MF and AuNPs and viewed along the [100] zone axis. Bottom: cryo-TEM image of the superlattices viewed along the [110] projection axis (scale bar, 25 nm). The panel also contains an image Fourier transform (top), inverse Fourier transform calculated with selected Fourier components (middle) and a unit cell viewed along the [110] projection axis (bottom).

capsid. The frame (left image) and surface (middle image) presentations in Fig. 3g–i show schematically the binding location of AuNPs viewed from different orientations. Comparison with experimental cryo-TEM tomography data shows that the positions of AuNPs that are in contact with the capsid match the model, indicating that the patchiness of the capsid can direct the formation of the AB_8^{fcc} superlattice (Supplementary Section S4).

The samples consisting of apoferritin (apoFT) and AuNPs were also found to self-assemble into binary nanoparticle superlattices (Fig. 4a). Similar to the CCMV assemblies, the formation of apoFT superlattices was critically dependent on κ^{-1}. SAXS curves in Fig. 4a (top) were measured at different κ^{-1} and show that superlattices are formed only when $\kappa^{-1} \approx 1.8-1$ nm. The one- and two-dimensional SAXS patterns clearly show the characteristics of an sc structure with $q^* = 0.508\ \text{nm}^{-1}$ and relative peak positions of $q^n/q^* \approx 1{:}\sqrt{2}{:}\sqrt{3}{:}2{:}\sqrt{5}$ corresponding to (100), (110), (111), (200) and (210) planes (Fig. 4a, bottom). Scattering is dominated by the AuNPs, which have a much higher electron density compared to the hollow cavity of apoFT. Here, the apoFT and AuNPs form two interpenetrating simple cubic structures (denoted as the (aFT–AuNP)^{sc} superlattice) with a $Pm\bar{3}m$ space group 221 and a lattice parameter a of 12.4 nm, which also equals the centre-to-centre distance between the apoFTs.

Superlattice structures almost identical to those formed with apoFT could be prepared from magnetoferritin (MF) at $\kappa^{-1} \approx 1$ nm (Fig. 4b, top). The difference with the MF superlattices is a slightly longer lattice parameter a (12.9 nm, corresponding to $q^* = 0.486\ \text{nm}^{-1}$). Otherwise the same (MF–AuNP)^{sc} particle configuration is observed (Fig. 4b, bottom). Here, scattering from the electron-dense iron oxide core of MF is also observed, corresponding to a structure that is isostructural with CsCl. The structure obtained by SAXS was verified by three-dimensional electron density maps from cryo-ET, which could be mapped with MF and AuNPs to yield a CsCl-type structure (Fig. 4c, top). Also, cryo-TEM images show the expected superlattice projections viewed along the [100], [110] and [111] zone axes (Fig. 4c, bottom and Supplementary Section S3). The observation of similar structures with apoFT and MF indicates that the protein cage is capable of directing the formation of the nanoparticle superlattices. In other words, different materials encapsulated into the FT cage can be assembled into analogous superlattices using this approach.

Under the experimental conditions where the FT superlattices form, the screening length is relatively short and the FT cage carries a negative net charge. The surface-to-surface distance between highly like-charged AuNPs is $>4\kappa^{-1}$, allowing the preferential formation of a relatively close-packed CsCl-type structure over NaCl and tetrahedral diamond lattices[5]. For FT and AuNPs, the size ratio is ~0.71, which is close to the optimum ratio of 0.73 at which the highest packing density for a CsCl-type lattice can be achieved. Furthermore, the locations of eight negative patches around the pores along the three-fold symmetry axes are, approximately, in a cubic arrangement, which may promote the formation of a CsCl lattice. As with CCMV, the FT-based superlattices do not form at pH values below the pI of FT or when the cage is covalently cationized (Supplementary Section S2).

The (MF–AuNP)^{sc} superlattices can withstand drying and are therefore not limited to a solution environment. Free-standing

superlattices can be prepared by magnetic separation and drying. The free-standing superlattices have the same structure and similar lattice constant as the hydrated assemblies. Finally, MF can function as a positive T_1 and negative T_2 magnetic resonance imaging (MRI) contrast agent. The MF superlattice structures are large and dense enough to provide an increase in the relaxivity rate compared to free MF particles (Supplementary Section S6).

In summary, we have shown that protein cages can guide the assembly of different materials into complex hierarchical structures. Three-dimensional binary superlattice structures were obtained by means of an optimized electrostatic assembly process where the interparticle interactions were controlled by tuning both the Debye screening length and pH. Specifically, the structure of the $(CCMV–AuNP_8)^{fcc}$ binary superlattice is unique in the sense that it has no atomic or molecular counterparts and has not been observed previously with nanoscale objects. AB^{sc}-type superlattices obtained with a FT cage show that the crystal structure is defined by the protein cage and not affected by the encapsulation of nanoparticles. Magnetic $(MF–AuNP)^{sc}$ superlattices obtained with iron oxide-loaded ferritin can be utilized as MRI contrast agents or free-standing superlattices. Protein cage-guided formation of nanoparticle superlattices provides a biocompatible platform that will facilitate the development of delivery and sensing applications in biological systems.

Received 28 August 2012; accepted 12 November 2012; published online 16 December 2012

References

1. Shevchenko, E. V., Talapin, D. V., Kotov, N. A., O'Brien, S. & Murray, C. B. Structural diversity in binary nanoparticle superlattices. *Nature* **439,** 55–59 (2006).
2. Macfarlane, R. J. *et al.* Nanoparticle superlattice engineering with DNA. *Science* **334,** 204–208 (2011).
3. Grzybowski, B. A., Wilmer, C. E., Kim, J., Browne, K. P. & Bishop, K. J. M. Self-assembly: from crystals to cells. *Soft Matter* **5,** 1110–1128 (2009).
4. Podsiadlo, P., Krylova, G., Demortière, A. & Shevchenko, E. Multicomponent periodic nanoparticle superlattices. *J. Nanopart. Res.* **13,** 15–32 (2011).
5. Kalsin, A. M. *et al.* Electrostatic self-assembly of binary nanoparticle crystals with a diamond-like lattice. *Science* **312,** 420–424 (2006).
6. Dong, A., Chen, J., Vora, P. M., Kikkawa, J. M. & Murray, C. B. Binary nanocrystal superlattice membranes self-assembled at the liquid–air interface. *Nature* **466,** 474–477 (2010).
7. Grzelczak, M., Vermant, J., Furst, E. M. & Liz-Marzán, L. M. Directed self-assembly of nanoparticles. *ACS Nano* **4,** 3591–3605 (2010).
8. Pileni, M-P. Self-assembly of inorganic nanocrystals: fabrication and collective intrinsic properties. *Acc. Chem. Res.* **40,** 685–693 (2007).
9. Nykypanchuk, D., Maye, M. M., van der Lelie, D. & Gang, O. DNA-guided crystallization of colloidal nanoparticles. *Nature* **451,** 549–552 (2008).
10. Park, S. Y. *et al.* DNA-programmable nanoparticle crystallization. *Nature* **451,** 553–556 (2008).
11. Brodin, J. D. *et al.* Metal-directed, chemically tunable assembly of one-, two- and three-dimensional crystalline protein arrays. *Nature Chem.* **4,** 375–382 (2012).
12. Cigler, P., Lytton-Jean, A. K. R., Anderson, D. G., Finn, M. G. & Park, S. Y. DNA-controlled assembly of a NaTl lattice structure from gold nanoparticles and protein nanoparticles. *Nature Mater.* **9,** 918–922 (2010).
13. Hu, M., Qian, L., Briñas, R. P., Lymar, E. S. & Hainfeld, J. F. Assembly of nanoparticle–protein binding complexes: from monomers to ordered arrays. *Angew. Chem. Int. Ed.* **46,** 5111–5114 (2007).
14. Sinclair, J. C., Davies, K. M., Venien-Bryan, C. & Noble, M. E. M. Generation of protein lattices by fusing proteins with matching rotational symmetry. *Nature Nanotech.* **6,** 558–562 (2011).
15. McMillan, R. A. *et al.* Ordered nanoparticle arrays formed on engineered chaperonin protein templates. *Nature Mater.* **1,** 247–252 (2002).
16. Aljabali, A. A. A., Lomonossoff, G. P. & Evans, D. J. CPMV-polyelectrolyte-templated gold nanoparticles. *Biomacromolecules* **12,** 2723–2728 (2011).
17. DuFort, C. C. & Dragnea, B. Bio-enabled synthesis of metamaterials. *Annu. Rev. Phys. Chem.* **61,** 323–344 (2010).
18. Srivastava, S. *et al.* Integrated magnetic bionanocomposites through nanoparticle-mediated assembly of ferritin. *J. Am. Chem. Soc.* **129,** 11776–11780 (2007).
19. Uchida, M. *et al.* Biological containers: protein cages as multifunctional nanoplatforms. *Adv. Mater.* **19,** 1025–1042 (2007).
20. De la Escosura, A., Nolte, R. J. M. & Cornelissen, J. J. L. M. Viruses and protein cages as nanocontainers and nanoreactors. *J. Mater. Chem.* **19,** 2274–2278 (2009).
21. Kewalramani, S. *et al.* Systematic approach to electrostatically induced 2D crystallization of nanoparticles at liquid interfaces. *Soft Matter* **7,** 939–945 (2011).
22. Okuda, M. *et al.* Fe_3O_4 nanoparticles: protein-mediated crystalline magnetic superstructures. *Nanotechnology* **23,** 415601 (2012).
23. Alloyeau, D. *et al.* Biotemplated synthesis of metallic nanoclusters organized in tunable two-dimensional superlattices. *J. Phys. Chem. B* **115,** 20926–20930 (2011).
24. Kostiainen, M. A. *et al.* Hierarchical self-assembly and optical disassembly for controlled switching of magnetoferritin nanoparticle magnetism. *ACS Nano* **5,** 6394–6402 (2011).
25. Kostiainen, M. A., Kasyutich, O., Cornelissen, J. J. L. M. & Nolte, R. J. M. Self-assembly and optically triggered disassembly of hierarchical dendron–virus complexes. *Nature Chem.* **2,** 394–399 (2010).
26. Hynninen, A. P., Christova, C. G., van Roij, R., van Blaaderen, A. & Dijkstra, M. Prediction and observation of crystal structures of oppositely charged colloids. *Phys. Rev. Lett.* **96,** 138308 (2006).
27. Meldrum, F., Heywood, B. & Mann, S. Magnetoferritin: *in vitro* synthesis of a novel magnetic protein. *Science* **257,** 522–523 (1992).
28. Glotzer, S. C. & Solomon, M. J. Anisotropy of building blocks and their assembly into complex structures. *Nature Mater.* **6,** 557–562 (2007).
29. Wang, Y. *et al.* Colloids with valence and specific directional bonding. *Nature* **491,** 51–55 (2012).
30. Gröschel, A. H. *et al.* Precise hierarchical self-assembly of multicompartment micelles. *Nature Commun.* **3,** 710 (2012).
31. Mani, E. *et al.* Sheet-like assemblies of spherical particles with point-symmetrical patches. *J. Chem. Phys.* **136,** 144706 (2012).
32. Velev, O. D. Self-assembly of unusual nanoparticle crystals. *Science* **312,** 376–377 (2006).
33. Leunissen, M. E. *et al.* Ionic colloidal crystals of oppositely charged particles. *Nature* **437,** 235–240 (2005).
34. Kowalczyk, B. *et al.* Size selection during crystallization of oppositely charged nanoparticles. *Chem. Eur. J.* **15,** 2032–2035 (2009).

Acknowledgements

This work was supported by the Academy of Finland (project 13137582), the Emil Aaltonen Foundation and an Aalto Starting Grant. P.C. thanks the Associazione Italiana per la Ricerca sul Cancro for funding (grant agreement MFAG10545) and the Italian Ministry of Economy and Finance for funding the Project 'FaReBio di Qualità'. This work made use of the Aalto University Nanomicroscopy Center (Aalto-NMC) premises. The authors thank J. van Lierop, O. Kasyutich, R. Nolte, J. Cornelissen, R. Sepponen, T. Lahtinen and S. van Dijken for discussions and support, and A. Nykänen for TEM support.

Author contributions

M.A.K. conceived the study and, together with P.H. and A.L., designed the experiments. P.H. contributed to SAXS measurements and cryo-ET data analysis. A.L. performed MRI measurements and data analysis. V.L. synthesized gold nanoparticles. J.S. and J.R. operated the TEM. P.C. prepared cationized magnetoferritin. M.A.K. performed all other experiments and wrote the paper. All authors discussed the results and commented on the manuscript.

Additional information

Supplementary information is available in the online version of the paper. Reprints and permission information is available online at http://www.nature.com/reprints. Correspondence and requests for materials should be addressed to M.A.K.

Competing financial interests

The authors declare no competing financial interests.